

Wearable Magneto-Inductive Waveguide for Low-Loss Wireless Body Area Networks

Vigyanshu Mishra, *Student Member, IEEE*, and Asimina Kiourti, *Senior Member, IEEE*

Abstract—A novel approach of wearable Magneto-Inductive Waveguide (MIW) is introduced for Wireless Body Area Network (WBAN) communications that brings forward significant advances over state-of-the-art. The MIW consists of series of electrically small resonant loops worn upon the human body to support Magneto-Inductive waves (MI waves) for low-loss/low-power WBANs. Compared to previous approaches, proposed MIW exhibits 63dB lower loss, translating conventional power levels of mW down to μ W or nW. In this work, we introduce operating principle of MIW WBAN through underlying theory and dispersion diagrams. Proof-of-concept numerical and experimental results are reported for frequency bands centered around 40.4MHz and 80.7MHz for a cylindrical human limb and are found to be in excellent agreement. Design guidelines are extensively discussed to accommodate several possible scenarios (frequency selection, gap between the loops, number of loops, and loop radius) along with practical considerations including loop tilts, anatomical limbs, limb movements, unequal loop gaps and loop failure. Specific Absorption Rate (SAR) calculations confirm that this technology is highly safe for human use. A bit error rate (BER) analysis further demonstrates that MIW can form a high quality communication channel for WBAN. Overall, the reported approach unveils a new possibility of low-loss and seamless WBANs.

Index Terms— Electrically small resonant loops, Magneto-Inductive Waveguide (MIW), Magneto-Inductive waves (MI waves), Wireless Body Area Network (WBAN).

I. INTRODUCTION

WEARABLE technology has seen remarkable growth in recent years, encompassing applications in the medical sector (e.g., measurement of physiological/vital signals [1], [2], body motion monitoring [1], [2], rehabilitation [1], [3]), consumer electronics [2], [3], gaming [1], [3], virtual reality [1], [3], and so on. Such wearable devices may be located on different parts of the human body and viewed as nodes. In turn, these nodes are generally connected to a hub/personal device (typically a mobile/smart phone) via wireless means [2], [4]. Such a wireless network is referred to as Wireless Body Area Network (WBAN) and may ultimately connect the

Manuscript received February 21, 2020; revised September 18, 2020; accepted September 20, 2020.

V. Mishra and A. Kiourti are with the ElectroScience Laboratory, Department of Electrical and Computer Engineering, The Ohio State University, Columbus, OH, 43212, USA (e-mails: mishra.186@osu.edu, kiourti.1@osu.edu).

TABLE I
COMPARISON OF STATE-OF-THE-ART WBANS VS. THE MIW APPROACH

	RF	HBC	MI	MIW (This work)
Path Loss	Very high	High	Low	Extremely low
Power	Very high	High	Low	Extremely Low
Channel Modeling	Highly variable and complex	Relatively less variable and complex	Variable and simple	Relatively less variable and simple
Reliability	Poor	Good	Good	Very good
Unobtrusive	Yes	No	Yes	Yes
Interference	Very high	No	Small	Negligible
Security	Low	Very high	Medium	High
Shadowing	Very high	Low	High	Low
Data Rate/Bandwidth	Low to extremely high	Low to high	Low	Low to very high

nodes, either directly or indirectly, to the Internet [1], [2]. That is, WBANs are the backbone of wearable technology. Its importance can further be gauged by the fact that any node malfunction would affect only that particular node (unless a network topology uses it otherwise), while a WBAN malfunction may impact the entire network/system. Hence, it is critical to build WBANs that are reliable and robust.

Referring to Table I, technologies reported to date for WBAN communications can be categorized into three types:

1) *Radio-Frequency (RF)*. RF WBANs (e.g., Bluetooth, BLE, ZigBee, and IEEE 802.15.6) are the most popular [1], [4], [5]. They integrate easily with existing wireless technology (e.g., mobile phones), are small in size, and achieve high data rates given their high operating frequency (401 MHz to 10.6 GHz [6]). However, RF WBANs suffer from (a) high path loss (caused due to RF radiation loss through tissues), (b) high power requirements (even the low-power ZigBee with a transmission output of 0 dBm and a data rate of 250 Kbps consumes a regular lithium battery in a few hours [4]), (c) complex channel modeling that compromises reliability (note that channel models change from one body part to another and as a function of the surrounding environment [1], [2], [6]), (d) interference caused by the presence of other devices operating in the same band, (e) security issues attributed to the interception of the constituent radiators, and (f) shadowing effect caused due to dynamic body movement (in the range of 30-40 dB) [5].

2) *Human Body Communication (HBC)* [5], [6] (also known

as Intra-body Communication (IBC), Body Centric Communication (BCC), or Body Channel Communication (BCC)). HBCs utilize the human body as the channel that transmits information (via capacitive or galvanic coupling [4], [6]), and utilize frequencies that are typically centered around 21 MHz (with bandwidth of 5.25 MHz) [4], [6]. Since the signal is confined in or in close proximity to the human body, they offer advantages in terms of security and interference [4], [6]. However, HBCs suffer from (a) high loss (though lower than RF WBANs [5], an example wrist-to-elbow HBC scenario still exhibits 45-55dB loss [5]), (b) high power requirements (\sim mW [4], as attributed to the electric field suffering loss through the human tissues), (c) complex channel modeling and poor reliability (given that human tissues, with time-varying dielectric, now form the channel), (d) bulkiness/obtrusiveness [5], and (e) safety concerns due to current flowing through the human body [4].

3) *Magnetic induction* [7]. This approach relies on magnetic coupling to transmit information between transmitter (Tx) and receiver loops placed upon the body. Though it overcomes issues associated with biological tissues (such as channel modeling), magnetic induction still suffers from high loss, especially as the distance between the transmitter and receiver increases. The latter is attributed to the inverse 6th power dependence with distance, and expectedly impacts the power requirements of these WBANs. Further, such dependence leads to significant performance degradation due to human body movement, akin to the shadowing effect in the case of RF WBANs. In addition to the above, magnetic induction typically supports low data rate/bandwidth [5].

To overcome shortcomings in the state-of-the-art, we propose a new approach of Magneto-Inductive Waveguide (MIW) for WBANs that relies on Magneto-Inductive waves (MI waves). MI waves were first demonstrated in [8] and have been an active topic of research since then. In our approach, MI waves are guided by an MIW formed by a series of electrically small resonant loops worn upon the body, Fig. 1. Since this method utilizes predominantly the magnetic field which has negligible effect due to biological tissues ($\mu_r \sim 1$), it eliminates concerns arising by the complex nature of human tissues, viz. complicated/unreliable channel modeling, high path loss, and safety concerns. Notably, because of its inherent wave-guiding nature, our MIW approach: (a) exhibits lower loss than even magnetic coupling, (b) reduces power requirements by several orders, (c) is not vulnerable to interference, (d) is highly secure, and (e) is minimally impacted by human body movement and shadowing. Concurrently, MIWs are capable of supporting low to very high data rates and bandwidth. Though copper wire implementations are targeted in this work, future designs may be realized on e-textiles to enable WBANs that are flexible, conformal, and unobtrusive. Such e-textile prototypes can be readily achieved, as confirmed by our prior work that demonstrates similar RF performance, for e-threads [9] and e-thread based sensors [10] with their respective copper counterparts.

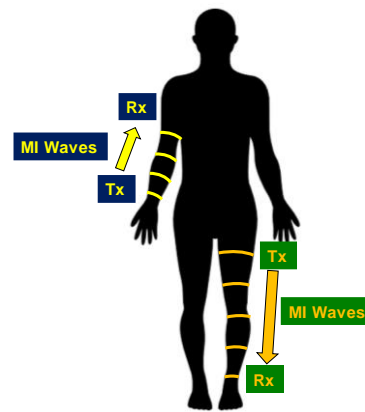


Fig. 1. Magneto-Inductive Waveguide (MIW) for WBANs.

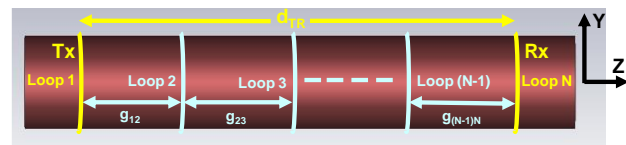


Fig. 2. Generic set-up of Magneto-Inductive waveguide (MIW) formed by electrically small resonant loops with transmitter (Tx) and receiver (Rx). Throughout this work, $g_{12} = g_{23} = \dots = g_{(N-1)N} = g$ is assumed, unless otherwise stated explicitly, and hence distance between Tx and Rx (d_{TR}) = $(N-1) \cdot g$.

Rest of the paper is organized as follows. In Section II, we introduce the operating principle of the MIW-based WBAN, discussing its underlying theory and demonstrating the dispersion diagram for an example set-up. To validate the concept, Section III presents numerical full-wave analyses and Section IV reports experimental analyses in two frequency bands of operation (centered around 40.4 MHz and 80.7 MHz, respectively). In Section V, design guidelines are laid out to meet different performance requirements for diverse WBAN applications. In Section VI, some practical considerations are discussed from a wearable perspective, such as effect of loop tilt, anatomical shape of limbs, limb movements, hypothetical non-uniform loop gaps, loop failure and discussion on preference of MIWs over continuous connecting structures (such as microstrip line). In section VII, the Specific Absorption Rate (SAR) performance of MIW is analyzed. This is followed by quantitative comparison of MIW vs. state-of-the-art approaches (RF, HBC, and magnetic induction based WBANs) in Section VIII. A bit error rate (BER) analysis is performed in Section IX to analyze the quality of communication channel and demonstrate low power consumption capability for MIW WBAN. The paper concludes in Section X.

II. OPERATING PRINCIPLE

As shown in Fig. 2, the proposed MIW WBAN consists of multiple single-turn electrically small resonant loops (each loaded with a capacitor), wrapped around the human limb with their axes aligned, and separated by a certain gap. As will be discussed next, this waveguide is capable of supporting MI waves. To understand the operating principle the setup of Fig. 2 is considered with a total of N loops. The analysis is inspired

from [11], and takes tissue loading into account. To simplify our analysis, it is assumed that: (a) the N^{th} loop is not acting as receiver (i.e., non-terminated, infinite line (i.e. $N \rightarrow \infty$) meaning no reflections), (b) all gaps are equal (i.e., $g_{12} = g_{23} = \dots = g_{(N-1)N} = g$), (c) all loops have equal radius, (d) the limb is approximated as a cylinder (e.g., arm or leg) with 2/3 muscle properties [12]–[14], (e) the axes of all loops and the limb axis align with the z-axis shown in Fig. 2, and (f) the plane of the loops is perpendicular to the z-axis. It is noted that all loops are electrically small and hence generate predominantly magnetic field when excited.

When Loop 1 acts as a transmitter (i.e., a voltage is applied across the loop), current is generated and a magnetic field is produced. This magnetic field gets linked to Loop 2 and generates current based on Faraday's law of induction. In turn, current is induced on the neighboring loops and the process continues until the current gets induced on the N^{th} loop (which will tend to zero as $N \rightarrow \infty$). That is, the process depicts a travelling phenomenon. In practice, induction occurs beyond just the neighboring element (although small). To simplify our analysis and to convey the operating principle clearly - without getting lost in details - we will hereafter consider the nearest neighbor approximation, i.e., a loop induces current only on its adjacent loop.

For any loop n (such that $1 < n \leq N$, where n and N are positive integers), the electrically small approximation allows us to apply Kirchhoff's Voltage Law (KVL):

$$I_n Z_n + j\omega M(I_{n-1} + I_{n+1}) = 0. \quad (1)$$

where, I_n is the current of the n^{th} loop, I_{n-1} and I_{n+1} (note that this term always exists because the line is infinite) are the currents induced on the $(n-1)^{\text{th}}$ and $(n+1)^{\text{th}}$ loops respectively (nearest neighbor approximation), M is the mutual inductance between two adjacent loops (same for all since the radius of all loops and gap in between is always the same), ω represents the operating angular frequency and Z_n represents the n^{th} loop impedance given by:

$$Z_n = R_n + j\omega L_n + \frac{1}{j\omega C_n} \quad (2)$$

where, R_n is the resistance of each loop (incorporating the wire resistance and the tissue loading effect), L_n is the self-inductance of each loop loaded by tissue, and C_n is the capacitance of the lumped capacitor added to the loop to make it resonant. Substituting (2) in (1) gives rise to a second order difference equation in space which has a form similar to the wave equation. Hence, the solution is of the form:

$$I_n = I_0 e^{-n\gamma g} \quad (3)$$

where, I_0 is a constant and $\gamma = \alpha + j\beta$ (γ is the propagation constant, α is the attenuation constant and β is the phase constant or wavenumber). Note that, unlike the electromagnetic wave solution which is continuous in free space, this solution is discrete because the medium through which current propagates (i.e., loops) is discretely located in

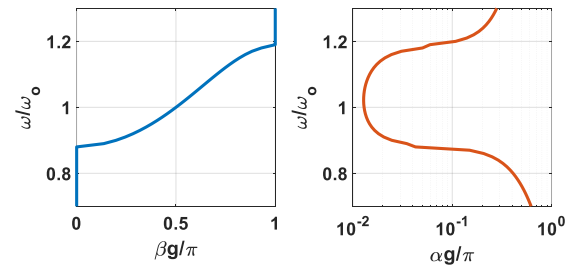


Fig. 3. Dispersion curves for a MI waveguide with electrically small resonant loops. This is obtained under assumption that the waveguide is not terminated (i.e. infinitely long waveguide) enabling a completely travelling wave.

space. Substituting (3) in (1) (and with (2) substituted in (1)) leads to the dispersion relation:

$$\left(\frac{\omega_0}{\omega}\right)^2 - 1 + \frac{j}{Q} = K \cosh(\gamma g) \quad (4)$$

where, $\omega_0 = 1/\sqrt{LC}$ is the resonant angular frequency of each loop (with L and C being the same for all loops and hence equal to L_n and C_n), $Q = \omega L/R$ is the quality factor of each loop, and $K = 2M/L$.

Equation (4) is a complex equation that consists of two independent equations (real and imaginary parts). The solution of these two equations provides the relation between ω/ω_0 vs. $\beta g/\pi$ and between ω/ω_0 vs. $\alpha g/\pi$, respectively. To plot the above, parameter values (i.e., R , L , C and g) are selected for an example set-up that will also be numerically and experimentally explored later in this paper. In doing so, analytical results can be correlated with our subsequent numerical and experimental results. Specifically, and referring to Fig. 2, loops of 4 cm in radius are considered, made of 30 AWG copper wire (diameter = 0.254 mm) and separated by a gap (g) of 2 cm. They are wrapped around a cylindrical human limb of 3.9 cm in radius made of 2/3 muscle [12]–[14]. Based on the above, parameter values are calculated as, $R=0.923\Omega$, $L=302.7\text{nH}$, $C=49\text{pF}$ and $g=2\text{cm}$.

Dispersion curves plotted using the aforementioned values are shown in Fig. 3. As seen, the passband ($0.88 < \omega/\omega_0 < 1.19$) and stopband ($\omega/\omega_0 \leq 0.88$ and $\omega/\omega_0 \geq 1.19$) associated with the MIW are quite clear. Results also set the theoretical limit of 31% on the fractional (percentage) bandwidth that can be obtained for this setup. Notably, Fig. 3 confirms the feasibility of creating a MIW on the human limb with significantly low loss/attenuation in the passband. Here, it is important to note that, if the analysis was performed in the absence of tissues, L and C would remain unchanged (electrically small approximation), but R would decrease to 0.58Ω . Thus, tissue loading will not affect the bandwidth and center frequency, but will cause slight change in loss/attenuation. Since the MIW approach utilizes predominantly the magnetic field and in a guided manner, it is possible to achieve significantly better performance over previous radiative or coupling mechanisms reported in the state-of-the-art.

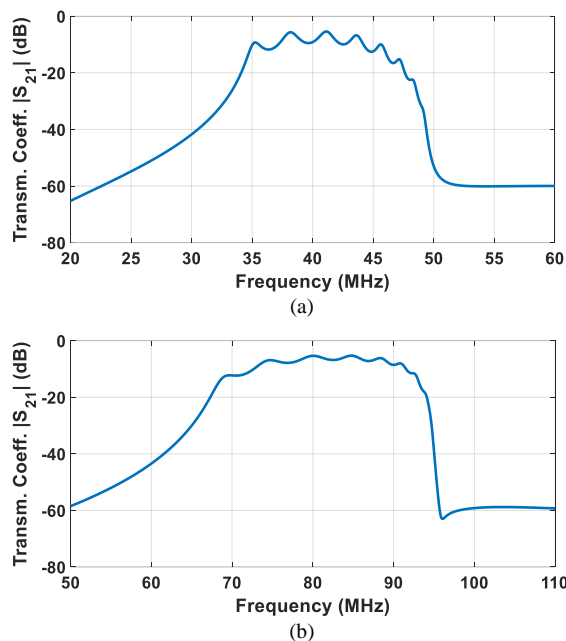


Fig. 4. Proof-of-concept $|S_{21}|$ full wave numerical results for $d_{TR}=20\text{cm}$ centered around (a) 40.4 MHz, and (b) 80.7 MHz.

III. NUMERICAL ANALYSIS

A. Numerical Setup

As a proof-of-concept and considering a practical scenario, the setup of Fig. 2 is employed with $N = 11$. Here, Loop 1 acts as a transmitter and Loop 11 acts as a receiver, i.e., the MIW is finite and terminated. Also, $g_{12} = g_{23} = \dots = g_{(10)11} = g = 2\text{ cm}$ such that the distance between transmitter and receiver is $d_{TR} = (N - 1) \times g = 20\text{ cm}$. The loop radius, wire diameter, and human limb diameter/material are same as those in Section II. Two frequency bands are selected for reasons that will become obvious in Section V.A: a) one that was used in Section II, i.e. around 40.4 MHz (deep inductive region), and b) one around 80.7 MHz (close to the edge of the inductive region). The lumped capacitors are selected as 49 pF (at 40.4 MHz) and 11.5 pF (at 80.7 MHz) to achieve resonance. For practical considerations and compatibility with measurement equipment, the port impedance of the transmitter and receiver are kept as $50\ \Omega$. That is, the MIW is excited and terminated by a finite impedance. Full-wave numerical simulations are performed using the frequency domain solver of CST Microwave Studio. Compared to the analytical method of Section II, it is expected that such numerical analysis will capture all realistic effects (i.e., finite length, waveguide termination with $50\ \Omega$, and interactions beyond the nearest neighbor approximation).

B. Numerical Results

Transmission coefficient ($|S_{21}|$) results as a function of frequency are shown in Fig. 4. Expectedly, $|S_{21}|$ values are analogous to the path loss or attenuation constant (α), while bandwidth is analogous to the passband described via the phase constant (β) in Fig. 3. Similarity in the trends of Fig. 3 and 4 is obvious, confirming the agreement between analytical

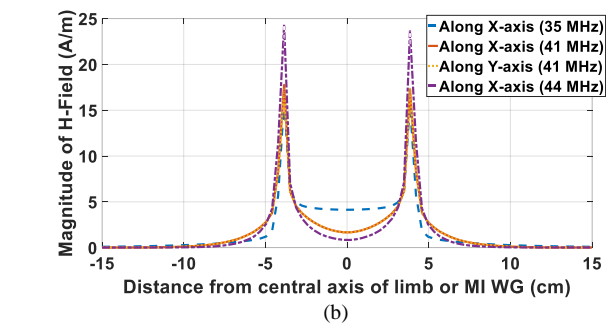
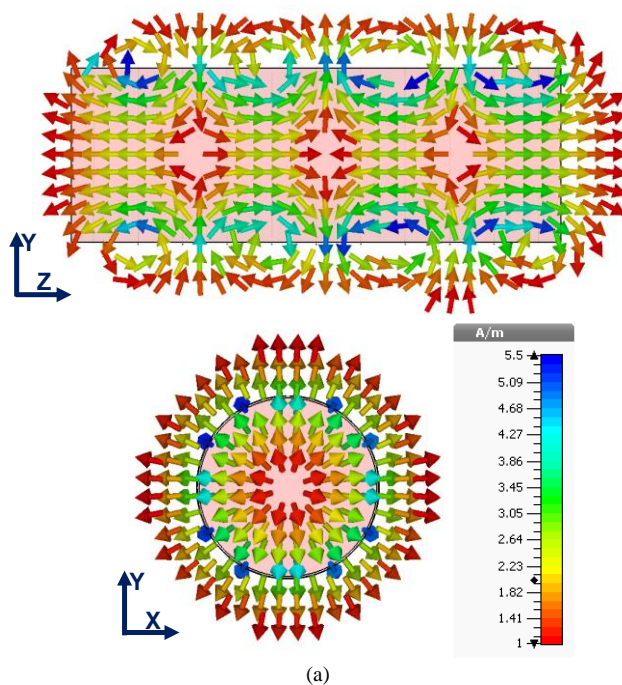


Fig. 5. H-field results within the 40.4 MHz band: (a) 2D plot of H-field along the waveguide (YZ plane per Fig. 2) at 41 MHz, and wave-guiding phenomenon (confinement of field) in XY plane at middle point along the length of the waveguide at 41 MHz, and (b) 1-D profile of magnitude of H-field at different frequencies within the band (and along the X and Y axis for 41 MHz) at middle point along the length of the waveguide.

and full-wave numerical results. Small differences arise out of non-idealities that were not considered in Section II. For example, ripples in the passband of Fig. 4 are mainly attributed to impedance mismatch; by contrast, the analysis of Fig. 3 assumed an infinite line without reflection. Here, it is worth noting that ideal matching implies a frequency-dependent terminating impedance [11]. As such, it is difficult to match the MIW across the band. Nevertheless, despite the inherent ripples, extremely low loss is achieved for the system (to be further improved in the future if the impedance matching problem is solved).

In the 40.4 MHz passband (Fig. 4(a)), a minimum path loss of 5.4 dB is obtained with an absolute 10 dB bandwidth of 11.8 MHz or fractional 10 dB bandwidth of 29.2% (lying within the 31% of theoretical limit obtained in Section II). In the 80.7 MHz passband (Fig. 4(b)), a minimum path loss of 5.3 dB is obtained with an absolute 10 dB bandwidth of 25 MHz or fractional 10 dB bandwidth of 30.9%. It is observed that absolute bandwidth increases with frequency while ripples

die down. The latter is attributed to reduced mismatch at higher frequencies. This is because tissue loading increases the resistance for frequency bands close to the edge of the inductive region.

For better visualization, Fig. 5(a) shows the 2-D H-field plot in the YZ-plane at 41 MHz (per the coordinate system defined in Fig. 2). Propagating MIW waves are clearly seen, along with a standing wave pattern formed due to impedance mismatch. Further, Fig. 5(a) also shows the H-field in the XY-plane at 41 MHz, while Fig. 5(b) shows a 1-D profile of the H-field at different frequencies within the 40.4 MHz band. The wave-guiding phenomenon is clearly evident in both Fig. 5(a) and (b) wherein most of the fields are concentrated around the edge of the waveguide (leading to least propagation inside tissue) and die down rapidly outside the guide. In addition, the 1-D field profile along the X-axis at three different frequencies (viz. 35, 41, and 44 MHz) in Fig. 5(b) indicates that the field intensity increases at the edges and decreases towards the middle as frequency increases. In all cases, the field drops close to zero within 5 cm of the edge of the MIW (where 4 cm is the MIW radius). Again, this clearly demonstrates the wave propagating and the wave-guiding phenomenon. Finally, results along the X-axis and Y-axis at 41 MHz are included in Fig. 5(b) to confirm that the field profile is identical in both cases (or would be in any direction in XY plane) due to the structural (circular) symmetry of the waveguide.

Although proof-of-concept results are demonstrated in this Section to confirm the feasibility of using MIW for WBANs, the performance results are by no way limiting. Ways to further improve certain performance metrics and/or translate the setup to different scenarios are discussed in Section V.

IV. EXPERIMENTAL ANALYSIS

A. Experimental Setup

Hollow cylindrical fixtures are 3-D printed to represent the human limb, Fig. 6(a). These are printed using clear resin so that all constituent materials/structures are visible. As will be discussed in Section V.A, the dielectric properties of the resin do not affect our measurements. Grooves are included within the fixtures to allow the electrically small resonant loops to be wrapped around and fixed at the designated gaps. Ground beef that has been used in the literature [15] to emulate the average human body properties is placed inside the fixture (Fig. 6(b)), thereby forming the complete set-up of Fig. 6(c). It is noted that the cylindrical fixture is composed of two parts to facilitate the beef insertion. All dimensions are identical to those of Section III, while 30 AWG copper wire and lumped capacitors are used to fabricate the resonant loops. SMA connectors are, finally, soldered at the two ends which are directly connected to a network analyzer PNA-L N5235A (Fig. 6(c)). Note that no balun is used here as the operating frequency band is inside the inductive (or non-radiative) region of operation. Two experimental setups are created, one for the frequency band centered around 40.4 MHz and the other for the frequency band around 80.7 MHz.

Here, it is worth noting that although our experimental setups are highly reliable, there are certain parameters which are prone to manufacturing defects (i.e., capacitance tolerance)

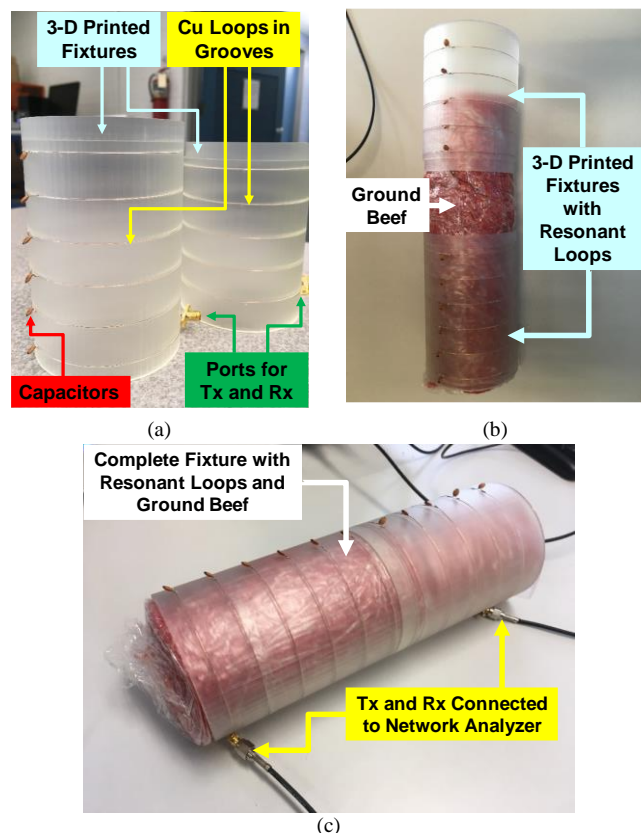


Fig. 6. (a) 3D printed cylindrical limb fixtures with grooves fitted with electrically small resonant loops at the designated gap, (b) two pieces of the fixture in the process of being combined together along with ground beef to emulate the human limb, and (c) complete set-up with Tx and Rx connected to a network analyzer.

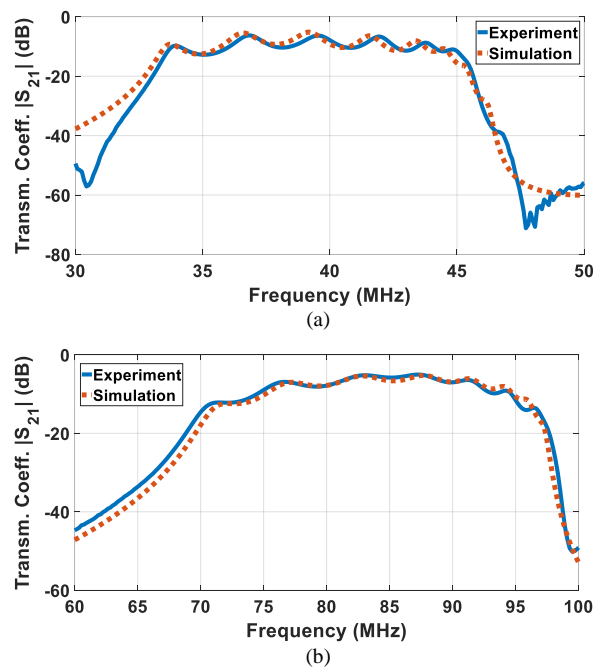


Fig. 7. Experimental and full wave numerical $|S_{21}|$ results centered around (a) 40.4 MHz and (b) 80.7 MHz.

and/or fabrication errors (i.e., radius of the resonant loops). Both these parameters were fine-tuned in simulation for optimal agreement with the corresponding experimental

results. In particular, the capacitance was fine-tuned by 0.75 pF for the 80.7 MHz band, while the loop radius was fine-tuned by 0.1cm for the 40.4 MHz band.

B. Experimental Results

Experimental $|S_{21}|$ results shown in Fig. 7 are in excellent agreement with the super-imposed simulations. Small differences can be attributed to variable tolerances of the capacitors and fine differences in loop radii across the waveguide. For the frequency band centered around 40.4 MHz, the minimum loss is 6.27 dB in measurements and 5.16 dB in simulations. Concurrently, an absolute 10 dB bandwidth of 12.15 MHz is observed in experiments as compared to 11.84 MHz in simulations. For the frequency band centered around 80.7 MHz, minimum loss of 5.03 dB and 5.24 dB is observed in experiments and simulations, respectively. The absolute 10 dB bandwidth is 27 MHz in experiments as compared to 26 MHz in simulations. These sets of proof-of-concept experimental results provide enough evidence on the feasibility of MIW for WBANs.

V. DESIGN GUIDELINES

This Section provides guidelines associated with MIW design, including selection of operating frequency, gap between the loops, number of loops, and loop radius. As will become evident, tuning these parameters is key to extending the distance between transmitter and receiver; translating the design upon different parts of the body and/or limbs of diverse individuals; meeting desired specifications in terms of loss, bandwidth, ripple behavior; and so on.

A. Selection of Frequency Band

Frequency band selection is associated with three major performance parameters: (a) effect of human tissues (ideally no or negligible effect is desired) (b) loss (ideally minimum), and (c) bandwidth (ideally maximum). To explore these aspects, the setup of Fig. 2 is considered using the parameter values of Section III, yet with capacitors tuned to each of the operating frequency bands under consideration. It is noted that the loop radius of 4 cm requires the operating frequency to be smaller than 120 MHz so as to ensure operation in the inductive region (based on a circumference of $< 0.1\lambda$).

To test the effect of human tissue properties (permittivity (ϵ_r) and loss tangent $(\tan\delta)$), two representative frequencies are considered: one inside the inductive region (80.7 MHz band) and one outside (276.4 MHz band). Since tissue properties differ among individuals and even for the same individual as a function of time, a $\pm 20\%$ [16] tissue property variation is hereafter considered from the nominal values (2/3 muscle). It is found that the 80.7 MHz band (Fig. 8(a)) exhibits negligible variation as compared to the 276.4 MHz band (Fig. 8(b)). This happens because loops inside the inductive region of operation predominantly use the magnetic field, and hence are negligibly affected by the presence of human tissue ($\mu_r \sim 1$). In fact, the 40.4 MHz band would exhibit negligible effect on performance even if the entire tissue limb was removed (Fig. 8(c)). Particularly, no shift in frequency, no change in bandwidth and a change of 2.6 dB in minimum path loss is observed, as predicted by the theoretical model of Section II.

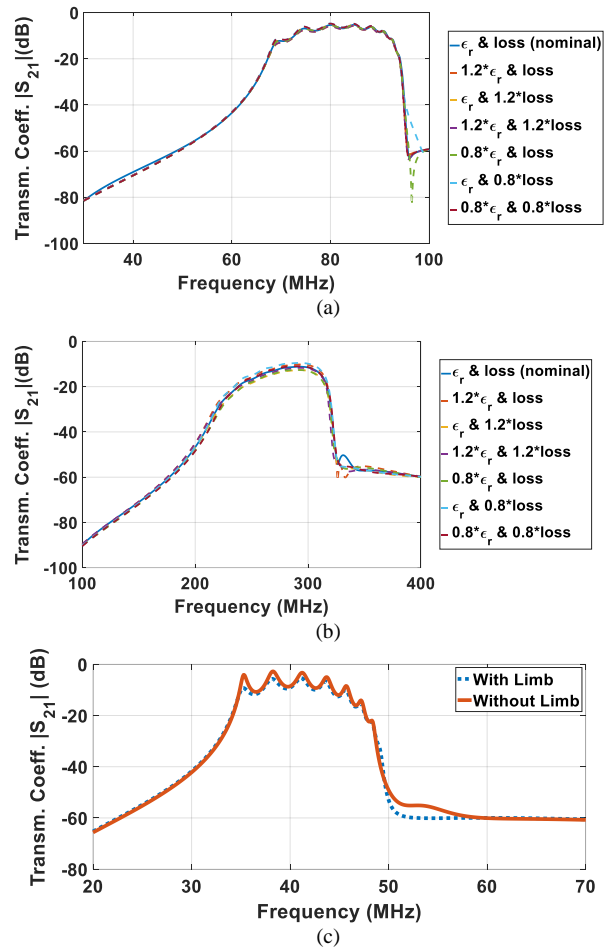


Fig. 8. Performance variability with change in tissue properties by $\pm 20\%$ for frequency bands centered around (a) 80.7 MHz and (b) 276.4 MHz. (c) Negligible change in performance in presence or absence of limb (tissue) for the 40.4 MHz frequency band.

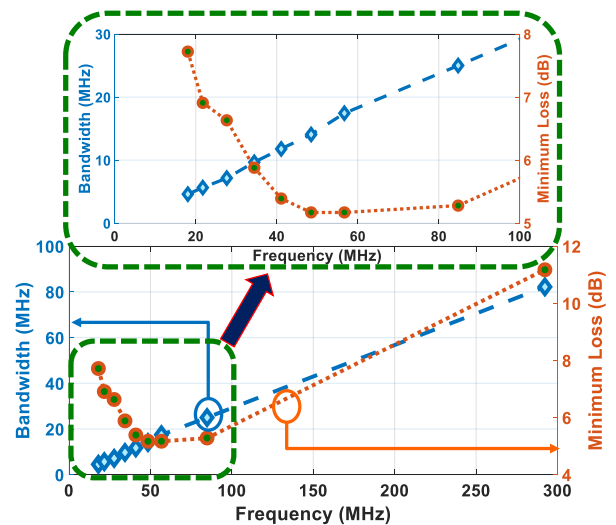


Fig. 9. Absolute 10-dB bandwidth and minimum loss variation with frequency. The inset depicts the trend specifically within the inductive region of operation.

As such, the inductive region of operation (preferably deep inductive region) is ideally suitable to realize MIW for WBANs.

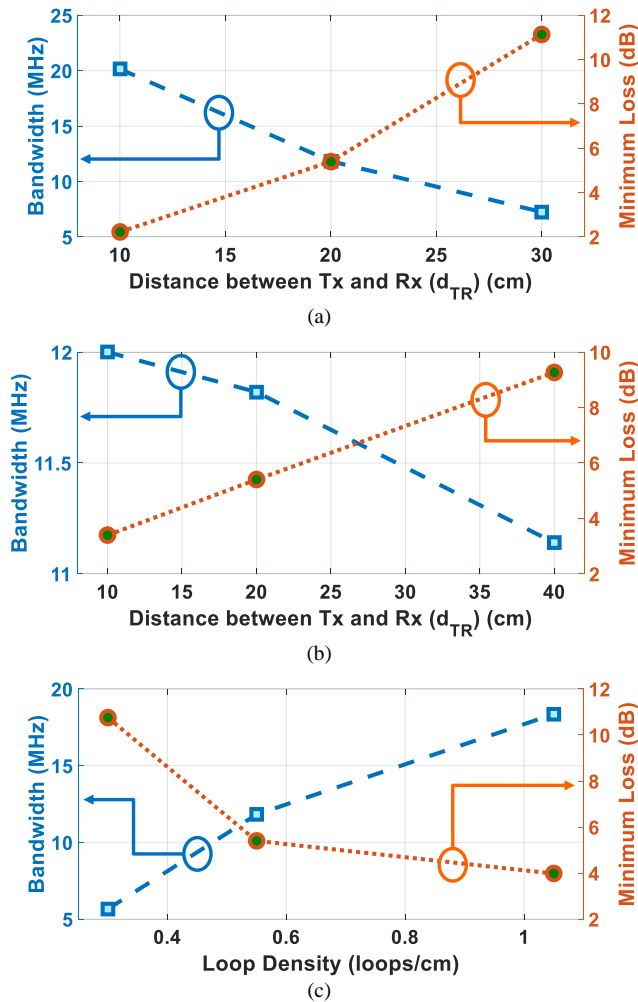


Fig. 10. Bandwidth and minimum loss in the 40.4 MHz band. (a) Distance between Tx and Rx increases by increasing ‘g’ while keeping the number of loops fixed. (b) Distance between Tx and Rx increases by increasing the number of loops while keeping ‘g’ fixed. (c) Increase in loop density such that the distance between Tx and Rx is fixed.

Numerical simulations are then carried out for nine different frequency points (eight of which lie in the inductive region, per the conclusion above). Fig. 9 plots the minimum loss and 10-dB absolute bandwidth for each of these frequencies. As seen, bandwidth is better for the frequency band outside the inductive region, however minimum loss is significantly higher. This behavior is attributed to radiative effects, i.e., losses seen by the electric field component, and further affirms that the inductive mode of operation (preferably deep inductive region) is preferred. However, if we look inside the inductive region, bandwidth increases monotonically with frequency, while loss hits a minimum and then increases again (Fig. 9). The latter behavior can be attributed to higher impedance mismatch at lower frequencies and radiation loss in tissues at higher frequencies that are close to the edge of the inductive region. Thus, for practical systems matched to 50Ω , where losses at lower frequencies may be high due to impedance mismatch and at higher frequencies due to radiation loss, a frequency in between can be chosen, as a tradeoff. This is yet another reason why the 40.4 MHz band was chosen for demonstration. In turn, the 80.7 MHz band was

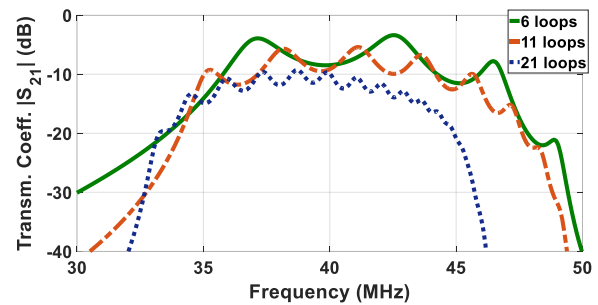


Fig. 11. Improved ripple behavior with increase in number of loops. $g=2$ cm, and hence, $d_{TR}=10$ cm (for $n=6$), 20cm (for $n=11$), and 40cm (for $n=21$).

chosen as the limiting case beyond which operation is not recommended. Note that these bands are for the specific design demonstrated in this work. Operating frequencies can change as per design, application and regulation requirements, however, guidelines towards band selection remain valid.

Added to the above, it is worth noting that the ripple effect increases with decrease in frequency (see Fig. 4 and 8). This is due to the combined effect of impedance mismatch and tissue loading. It is also interesting to note that the operating principle described in Section II is valid under the assumption of electrically small loops; hence operation inside the inductive region is in congruence with the analysis of Section II which can be leveraged to optimize the system design.

B. Selection of Gap and Number of Loops

Selection of gap and number of loops can be analyzed in three different ways: (a) gap between the loops is uniformly increased while the number of loops is kept fixed, such that the distance between transmitter and receiver (d_{TR}) increases, (b) increase in number of loops while the gap is kept fixed, such that d_{TR} increases, and (c) increase in loop density (i.e., number of loops per unit length), such that the number of loops increases while d_{TR} remains fixed. All subsequent analyses are conducted in the 40.4 MHz frequency band.

Considering scenario (a), the set-up of Fig. 2 is used per Section III and the gap between the loops is increased from 1 cm ($d_{TR} = 10$ cm) to 3 cm ($d_{TR} = 30$ cm) with a step of 1 cm. Results are summarized in Fig. 10(a) indicating that bandwidth decreases and minimum loss increases as d_{TR} increases. Hence, d_{TR} can be increased by increasing the gap and keeping the number of loops fixed, but at the cost of reduced bandwidth and increased loss. For scenario (b), three set-ups are studied with $N = 6, 11$ and 21, while the gap is fixed at $g = 2$ cm. This leads to three values for d_{TR} , viz. 10 cm, 20 cm, and 40 cm. Referring to Fig. 10(b), again bandwidth decreases and minimum loss increases as d_{TR} increases. Nevertheless, the decrease in bandwidth is significantly less relative to scenario (a), while the increase in minimum loss is also smaller compared to scenario (a). Depicted in Fig. 11 is the $|S_{21}|$ response for each scenario, showing that the ripple peak-to-peak variation also reduces with increasing number of loops, as strongly desired. Hence, increasing the number of loops is a better way of increasing d_{TR} . To explore scenario (c), the same number of loops is used as in scenario (b), while the gap between the loops is set to 4 cm (for $N = 6$), 2 cm (for $N = 11$), and 1 cm (for $N = 21$). In

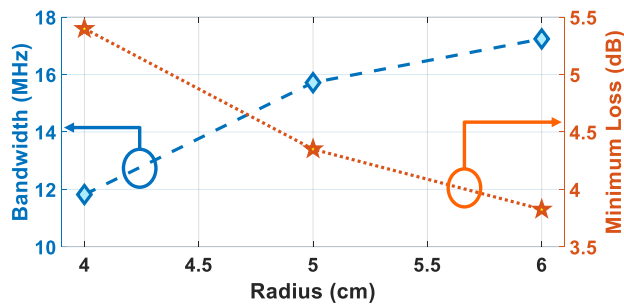


Fig. 12. Absolute bandwidth increases while minimum loss decreases (both desired) as radius increases. This setup assumes $g = 2$ cm and 11 loops, resulting in $d_{TR} = 20$ cm.

doing so, d_{TR} remains fixed at 20 cm. As seen in Fig. 10(c), higher loop density is desirable as it provides lower minimum loss and higher bandwidth.

In summary, higher loop density and increased number of loops are recommended for larger distances between the transmitter and receiver. Should this not be feasible in practical situations, the aforementioned tradeoffs have to be kept in mind.

C. Radius Selection

To explore the effects of radius selection (to enable design on different limb sizes), the set-up of Fig. 2 is considered. Parameter values are the same as in Section III for 40.4 MHz band, except the radius of the loop and limb vary per case. Three different radii (4 cm, 5 cm and 6 cm) are considered in our studies and results are summarized in Fig. 12. As seen, bandwidth increases and minimum loss decreases with increasing radius. It is also observed that ripples tend to smooth out as radius increases. It is interesting to observe that increasing radius has some equivalence to increase in frequency. This is because an increase in radius pushes the edge of the inductive region towards lower frequencies.

VI. SOME PRACTICAL CONSIDERATIONS

This section focusses on certain practical considerations of MIW WBAN and their effect on the associated performance. These include: (a) tilt of the loops, (b) change in radius due to the anatomical limb, corresponding capacitor tuning requirements, (c) limb movements including bending/flexion, and rotation across joints and unequal gap between loops caused due to such movements, (d) hypothetical and random non-uniform gap between loops, (e) loop failure leading to break in the waveguide, and their possible impact on performance (mainly in terms of path loss, bandwidth or/and shift in center frequency). Finally, we explore why we cannot use a continuous connecting structure instead of a discrete structure such as MIW.

A. Effect of Tilt

In a practical setting, loops of MIW WBAN will be integrated in garments and the plane of the loop may tilt (θ_t - see Fig. 13(a)) rather than being completely transverse to the axis of the limb (Fig. 2 and Fig. 6). To understand the effect on performance, three different scenarios are considered: (a) no tilt ($\theta_t = 0^\circ$ for all loops) (Fig. 2), (b) uniform tilt ($\theta_t = 10^\circ$

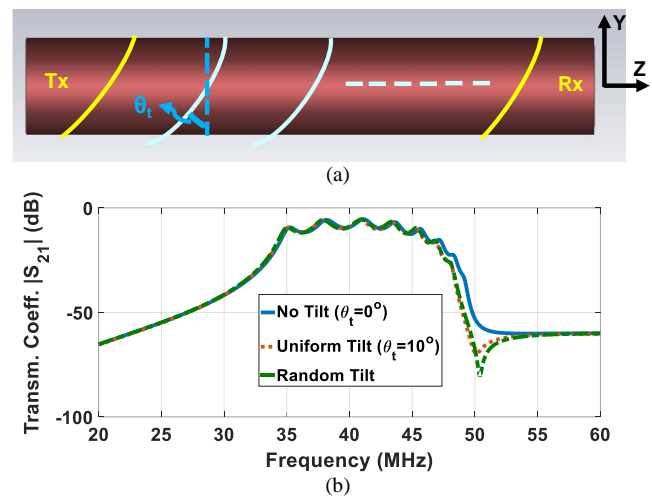


Fig. 13. (a) Depiction of loop tilt (θ_t) in MIW, and (b) $|S_{21}|$ result for 40.4 MHz band MIW corresponding to three different scenarios, viz. no tilt ($\theta_t = 0^\circ$ for all loops) – same as result of Fig. 4(a), uniform tilt ($\theta_t = 10^\circ$ for all loops), and random tilt ($\theta_{t1} = 5^\circ, \theta_{t2} = 2^\circ, \theta_{t3} = -1^\circ, \theta_{t4} = 10^\circ, \theta_{t5} = -4^\circ, \theta_{t6} = 1^\circ, \theta_{t7} = 7^\circ, \theta_{t8} = -6^\circ, \theta_{t9} = 3^\circ, \theta_{t10} = 0^\circ, \theta_{t11} = -8^\circ$).

for all loops) (Fig. 13 (a)), and (c) random tilt ($\theta_{t1} = 5^\circ, \theta_{t2} = 2^\circ, \theta_{t3} = -1^\circ, \theta_{t4} = 10^\circ, \theta_{t5} = -4^\circ, \theta_{t6} = 1^\circ, \theta_{t7} = 7^\circ, \theta_{t8} = -6^\circ, \theta_{t9} = 3^\circ, \theta_{t10} = 0^\circ, \theta_{t11} = -8^\circ$). Note that, with $\theta_t = 0^\circ$, the ‘no tilt’ design is same as the proof-of-concept design with 11 loops, $g = 2$ cm, and centered at frequency of 40.4 MHz of Section III. ‘Uniform tilt’ and ‘random tilt’ designs are variants (with changed θ_t) of the abovementioned proof-of-concept design and signify two different and possible representative practical scenarios. Note that variation within $\pm 10^\circ$ is quite practical for stretchy clothing that lies close to the skin [17].

Results for all three designs are summarized in Fig. 13(b) depicting negligible change in performance due to tilt. Particularly, for uniform tilt and random tilt, we observe increase of minimum path loss by 0.22 dB and 0.02 dB respectively, decrease in bandwidth by 0.15 MHz and 0.06 MHz respectively, and shift (decrease) in center frequency by 0.23 MHz for both compared to the no tilt design. Hence, the design would be quite robust to possible loop tilts in practical scenarios.

B. Effect of Anatomical Shape of the Limb

Practically, limbs are not perfectly cylindrical, thereby making it important to understand the effect of anatomical shape on the performance of MIW WBAN. For this, a conical approximation (a closer approximation to anatomical shape) of the limb is made. An 11-loop MIW WBAN is designed on this limb with loop radii varying from 6 cm (transmitter end) to 4 cm (receiver end) with a step size of 0.2 cm and separated by a gap (g) of 2 cm (see Fig. 14(a)). Note that all design parameters (except radius) are the same as those of the proof-of-concept design of Fig. 2 centered around 40.4 MHz.

Change in radius would cause change in inductance of each loop, thereby requiring different value of capacitance for each loop to make all loops resonate at same frequency. This would ideally require a fine tuning for each loop. In practical settings, this would not be impossible, but would require more time and effort. Hence, an approach of uniform distribution can be used instead. Here, only transmitter and receiver are

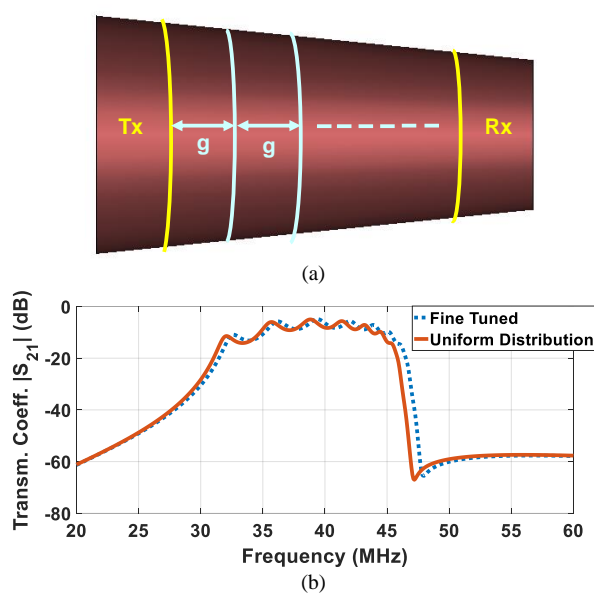


Fig. 14. (a) Conical approximation of anatomical limb with varying radius 11-loop MIW WBAN such that radius of loops vary from 6 cm (Tx) to 4 cm (Rx) with step size of 0.2 cm and $g = 2$ cm. (b) Results corresponding to the ideal case of fine tuning each loop with different capacitance and a practical approach of uniform distribution where only transmitter and receiver require fine tuning with rest of the loops in between following uniform distribution for capacitance values.

tuned and the capacitance value for loops in between can be determined using the uniform distribution as follows:

$$C_{step} = \frac{|C_{Tx} - C_{Rx}|}{N-1} \quad (5)$$

where, C_{step} represents the step change in capacitance value from one loop to next, C_{Tx} and C_{Rx} represent fine-tuned transmitter and receiver capacitances respectively, and N represents the total number of loops.

The result for both fine-tuned and uniform distribution designs is shown in Fig. 14(b). As seen, there is negligible difference in performance. Particularly, the minimum path loss increases by 0.11 dB, bandwidth reduces by 0.15 MHz, and center frequency shifts by 0.55 MHz. These results show that it is possible to implement the MIW WBAN on anatomical shaped limbs. Also, they demonstrate a more practical and easy way of tuning the capacitance with negligible change in performance. Note that this approximation is by no way restricted to just uniform distribution and it is possible to use other types of distributions which may fit better with a given situation or anatomical shape of limb.

C. Effect of Limb Movements

MIW-enabled wearable WBANs will be inevitably impacted by human movement. Here, we consider common human movements that involve bending (or flexion) and rotation of limbs (arm/leg) across the joints (elbow/knee). For this, the set-up of Fig. 2 is used with 11 loops centered around 40.4 MHz and bending/flexion and rotation are integrated (see Fig. 15(a)). Flexion happens about the center of joint C, forming a flexion angle of θ_f . Rotation happens about the limb's own axis (also known as pronation/supination in the case of arm and internal/external rotation in the case of knee) as shown in Fig. 15(a). Simulation results for $\theta_f = 0^\circ$ to 25° (allowed range of motion) with a step-size of 5° are shown in Fig. 15(b). As seen, there is negligible effect on performance

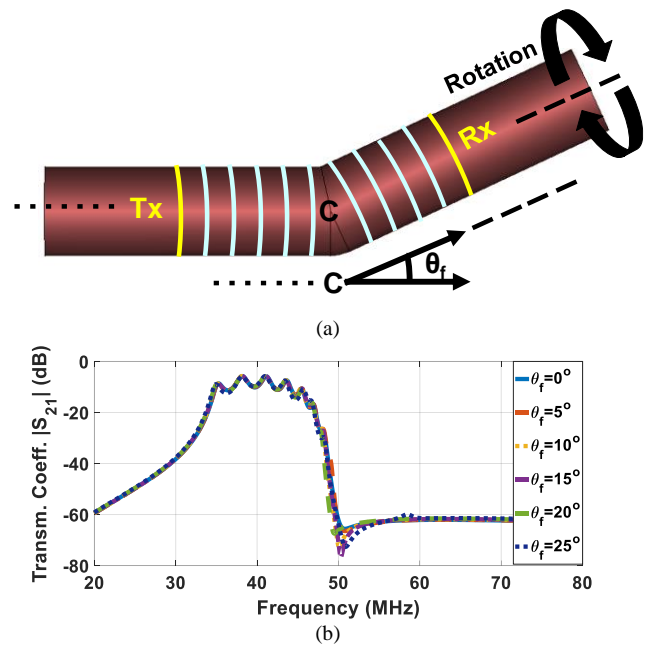


Fig. 15. (a) Set-up of 11 loop MIW WBAN corresponding Fig. 2 centered around 40.4 MHz implemented on a limb across the joint (elbow/knee). Limb can bend/flex across the center of joint C with a flexion angle θ_f . (b) Results for $\theta_f = 0^\circ$ to 25° demonstrate negligible effect of limb bending on MIW performance.

due to flexion/bending of limbs. Particularly, maximum changes of +0.05 dB (+0.87%) in minimum path loss and +0.95 MHz (+8.1%) in bandwidth are observed. Another simulation result for a 6-loop MIW WBAN with $g = 4$ cm shows similar results, wherein the performance has negligible effect for $\theta_f = 0^\circ$ to 50° with a step-size of 5° . This can be attributed to the fact that loops tend to diverge apart at the joint on one end but come closer on other end (see Fig. 15(a)), thus not having much effect on the coupling. In fact, coupling gets improved because the effective distance between the loops on the transmitting and receiving ends tends to decrease, thus slightly improving the path loss and bandwidth. Note that, beyond certain θ_f , some loops may physically touch each other, which requires *in vivo* testing in future and cannot be simulated. However, the above will lead to either direct connection or increased coupling that will also tend to improve the performance. For rotation simulations, the performance remains unaltered as attributed to the inherent rotational symmetry of the MIW configuration. Hence, under such dynamic settings, the performance of wearable MIW would either remain unaffected (or negligibly affected) or would tend to improve, but not degrade.

Fig. 15(a) also denotes a realistic scenario where loops may get unequally spaced (see gap between the loops at the joint). Apart from such scenarios, unequal gap and misalignment/tilt (covered in Section VI.A) can also occur due to stretching or deformation of the clothing caused due to dynamic movements [17]. Any such change in gap (both increase and decrease) would change the performance metric of the MIWs and could be predicted by Fig. 10(a). For instance, [17] shows that the initial displacement for stretchy fabrics is ~ 2.1 cm when the limb bends from $\theta_f = 0^\circ$ to 90° multiple times. Note that this initial displacement is towards the joint, and hence would reduce the gap between the loops which would further

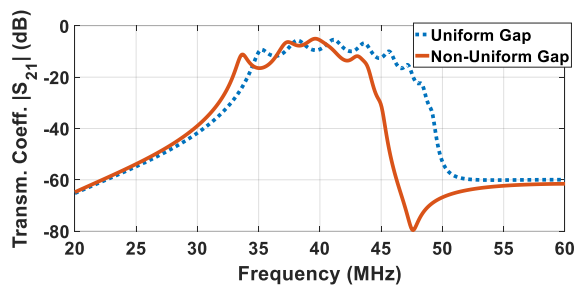


Fig. 16. Effect on performance due to random and hypothetical non-uniform gap vs. uniform gap of Fig. 4(a). For non-uniform gap 11 loops are considered in Fig. 2 with $g_{12}=1.5\text{cm}$, $g_{23}=2.3\text{cm}$, $g_{34}=2.4\text{cm}$, $g_{45}=2.3\text{cm}$, $g_{56}=1.3\text{cm}$, $g_{67}=2.5\text{cm}$, $g_{78}=1\text{cm}$, $g_{89}=2.3\text{cm}$, $g_{9(10)}=3\text{cm}$, $g_{(10)(11)}=1.4\text{cm}$.

improve the performance of MIW per Fig. 10(a). Once initially displaced, the fabric shows negligible displacement [17] and so will the performance of MIW. Such fabrics are an ideal candidate for the initial implementation of wearable MIWs. In another instance, it is possible that the gap between the loops may increase and hence the performance will degrade as per Fig. 10(a). In addition to the above, it must be noted that, unequal gap caused due to deformation or stretching could also mean both increase in gap (reduced coupling) for some loops and decrease in others (improved coupling). Such changes could neutralize each other, thereby resulting in either no change or negligible change in performance. However, more realistic and elaborate *in vivo* studies for different types of movements are needed to say anything conclusively.

D. Effect of Hypothetical and Random Non-Uniform Gap

This section covers unforeseen scenarios related to gap between the loops that are not covered in Section VI.C, but may occur in wearable and dynamic cases. For this, a hypothetical and random non-uniform gap is created on the set-up of Fig. 2 (corresponding result of Fig. 4(a)). Referring to Fig. 2, $g_{12}=1.5\text{cm}$, $g_{23}=2.3\text{cm}$, $g_{34}=2.4\text{cm}$, $g_{45}=2.3\text{cm}$, $g_{56}=1.3\text{cm}$, $g_{67}=2.5\text{cm}$, $g_{78}=1\text{cm}$, $g_{89}=2.3\text{cm}$, $g_{9(10)}=3\text{cm}$, $g_{(10)(11)}=1.4\text{cm}$. The result obtained is plotted alongside the result of Fig. 4(a) (uniform gap, $g=2\text{cm}$) and is shown in Fig. 16. As seen, the performance degrades, particularly, in terms of bandwidth. Hence, although considered as a hypothetical scenario, the results depict a constraint that needs to be taken into account if such non-uniform gap cases are encountered. In future, the above can be confirmed and ultimately resolved via *in vivo* studies.

E. Effect of Loop Failure

Loops of MIWs may become non-functional in practical situations due to breaking of the loop itself or the capacitor, among other possibilities. This would cause a break in the waveguide structure. One such scenario is simulated for the set-up of Fig. 2 with 11 loops centered around 40.4 MHz but with a broken/missing loop in the middle of the waveguide. Results are summarized in Fig. 17. As seen, the performance degrades due to loop failure or break in the waveguide. However, the impact is not severe and the waveguide will still remain operational. Note that, the nature of performance degradation will be a function of the location of loop failure across the waveguide, but the impact will not be severe in any

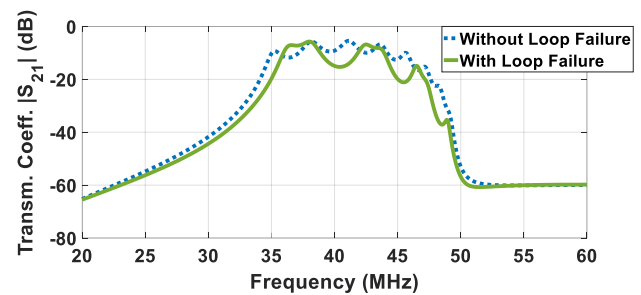


Fig. 17. Effect of loop failure or broken waveguide on 11 loop MIW design of Fig. 2 centered around 40.4 MHz. The performance gets affected, however, the effect is not as severe as would be for any other traditional continuous wave-guiding structure.

case. Also, as expected, the performance degradation caused due to loop failure can be ameliorated by having higher loop density (see Fig. 10(c)) in MIWs. Finally, in case of multiple loop failures, the MIWs may become non-operational. Although, above may seem like a constraint, it must be remembered that MIWs will ultimately be integrated in clothes via e-threads which have significantly high mechanical strength, thereby reducing the probability of loop failure manifolds. Hence, e-textile version of MIWs will be relatively robust structures with respect to any break in the waveguide and hence quite suitable for wearable WBANs.

F. Why not a continuous connecting structure?

A continuous connecting structure, such as an e-textile based microstrip line (a wave-guiding structure) at high frequencies or a direct connection via an e-textile based conductor at low frequencies, could be an alternative to the proposed MIW-based WBAN. Such continuous structures would have even better path loss and bandwidth (especially at high frequency) compared to MIWs. However, there are several reasons why MIWs are still preferable for wearable WBAN. For instance: (a) A single piece of cloth would be needed for a continuous connection throughout the body which is not practical; by contrast, MIWs allow for different pieces of cloth across different body parts without loss in connection. (b) A continuous connection will have to run all across the link, including joints, which would lead to frequent wear and tear and could eventually break the connection and lead to complete failure besides possibly restricting the natural movement; by contrast, MIWs can easily circumvent such locations on the body due to their inherent discrete nature (see Fig. 15(a)). (c) If a connection breaks at a place other than that mentioned in (b) above, it might affect the continuous structure and MIW alike. In such cases, the continuous structure would again see a severe degradation in performance or even complete loss of signal; by contrast, the impact in case of loop failure for MIW would be significantly less severe (refer to Section VI.E and Fig. 17) thereby keeping the connection intact. (d) Integration of a new node in WBAN formed via a continuous structure would be troublesome due to the necessity of physical connection. Also, such physical connections are more prone to breaks in a wearable scenario, while removing the node would require removal of a physical connection hence adding to the hassle and making the system user-unfriendly. By contrast, MIW WBAN allow easier integration of any new node (Tx/Rx) wirelessly without any hassle of physical connection. For instance, a mobile phone

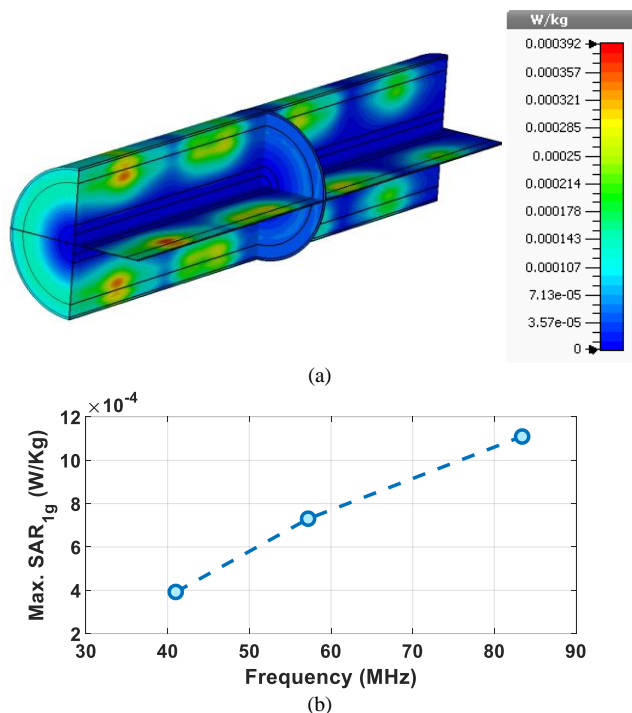


Fig. 18. (a) SAR_{1g} distribution in different planes (cross-sections) at 41 MHz and 1 mW input power. (b) Maximum SAR_{1g} variation with frequency assuming 1mW input power.

(node) can be connected to the MIW via its inbuilt near field communication (NFC) technology.

VII. SPECIFIC ABSORPTION RATE STUDIES

Electromagnetic safety is one of the most important design criteria before any wireless technology can be practically deployed. To this effect, a Specific Absorption Rate (SAR) study is hereafter presented for MIW-based WBANs. For more realistic results, a multi-layer limb model [10] is used, consisting of skin, fat, muscle, cortical bone, and bone marrow. The setup of Fig. 2 is employed with parameter values same as in Section III, except that capacitances are tuned per frequency scenario. Three frequency bands are considered, viz. 40.4 MHz, 56.9 MHz, and 80.7 MHz, and SAR results averaged over 1 g of tissue (SAR_{1g}) are shown in Fig. 18.

Specifically, Fig. 18(a) shows the SAR_{1g} distribution upon different cross-sections at 41 MHz. For an input power of 1 mW, the maximum SAR_{1g} is 0.000392 W/Kg. This is significantly less than the 1.6 W/Kg limit set by the Federal Communications Commission (FCC) [18]. Note that the chosen input power of 1 mW is still high for WBAN; it is considered here as prescribed by IEEE 802.15.6 as maximum reference power [3]. To demonstrate the effect of increasing frequency on SAR, Fig. 18(b) shows the increase of SAR_{1g} with increasing frequency for an input power of 1 mW. Even so, to reach the maximum SAR_{1g} limit of 1.6 W/Kg at the highest frequency band of 80.7 MHz, an input power of 1W is required (impractically high for WBAN applications). In any case, the results of Fig. 18(b) further highlight why lower frequencies are to be preferred and confirm that MIW-based WBANs are highly safe for human use.

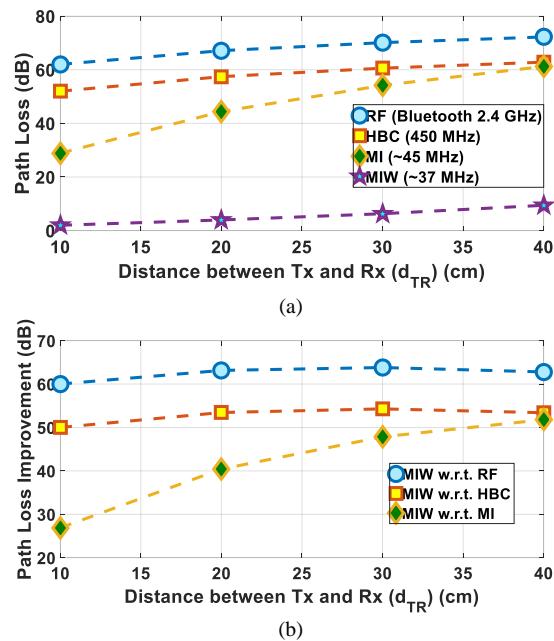


Fig. 19. (a) Path loss variation with distance for state-of-the-art technologies and MIW, and (b) Improvement in MIW based WBAN with respect to (w.r.t.) state-of-the-art.

VIII. COMPARISON WITH STATE-OF-THE-ART

In order to perform a quantitative comparison vs. the state-of-the-art, four set-ups are considered for WBANs operating based on: (a) Radio Frequency (RF), (b) Human Body Communication (HBC), (c) Magnetic Induction (MI), and (d) Magneto-Inductive Waveguide (MIW). For the RF and HBC WBANs, the work in [19] is used as reference. As such, this study calculates the path loss for RF (Bluetooth nodes operating at 2.4 GHz) and HBC (at 450 MHz) on the left arm with varying distance between the transmitter and receiver, which is further fit using the following model:

$$P_{dB} = P_0 - 10n \cdot \log_{10} \left(\frac{d}{d_0} \right) + N(0, \sigma_p) \quad (6)$$

where, P_{dB} is the path loss (to be calculated), P_0 is the path loss for a reference distance of $d_0=10\text{cm}$, n is the path loss exponent and N is the lognormal variance on path loss (ignored for comparison here). Using this model, the path loss for both RF ($P_0 = -62$ dB and $n = 1.7$) and HBC ($P_0 = -52$ dB and $n = 1.8$) WBAN is calculated for d (or d_{TR}) = 10 cm to 40 cm at step of 10 cm. For the MIW WBAN, the setup of Fig. 2 is used with $N = 21$ and $g = 0.5\text{cm}, 1\text{cm}, 1.5\text{cm}$ and 2cm so as to realize $d_{TR} = 10$ cm to 40 cm in steps of 10cm. For the magnetic induction WBAN, the aforementioned setup is considered yet with only the transmitter and receiver loops (i.e., no loops in between).

Plots of path loss (Fig. 19(a)) and path loss improvement (Fig. 19(b)) for MIW with respect to RF, HBC, and MI based WBAN as a function of distance between the transmitting (Tx) and receiving (Rx) loops clearly confirm the magnitude of improvement. Path loss improves by over 60 to 63 dB, 50 to 54 dB, and 26 to 51 dB as compared to RF, HBC, and MI based WBAN, respectively, within d_{TR} of 10cm to 40cm. Notably, the improvement becomes more prominent as the

distance increases (specifically more visible in the case of MI). These results can directly translate to improvements in terms of power requirements, i.e., conventional ~mW power requirements can now reduce to μW or nW (further elaborated in Section IX quantitatively). Note that this kind of improvement is achieved with just proof-of-concept results, and further optimization is feasible in the future.

IX. BIT ERROR RATE

In this Section, bit error rate (BER) is used to characterize the communication capability of the MIW for WBAN. This analysis also helps to quantitatively understand how improvement in path loss can help bring conventional ~mW power levels to orders of μW or nW for MIW WBAN.

Under the assumption of only thermal noise, MIW WBAN can be assumed to form an additive white Gaussian noise (AWGN) channel. Also, because thermal noise is inherently incoherent, the total thermal noise power associated with the MIW WBAN ($P_{n,MIW\ WBAN}$) can be given by,

$$P_{n,MIW\ WBAN} = NkTB \quad (7)$$

where N is total number of loops used in the MIW WBAN, k is Boltzman constant ($1.38 \times 10^{-23} \text{ m}^2 \text{ kg s}^{-2} \text{ K}^{-1}$), T is temperature, and B is bandwidth. Considering the MIW WBAN proof-of-concept design of Section III centered around 40.4 MHz at room temperature, leads to $N=11$, $T=300\text{K}$, and $B=11.8\text{MHz}$. These values yield $P_{n,MIW\ WBAN}=-92.7 \text{ dBm}$. Next, the output signal to noise ratio for MIW WBAN can be calculated by,

$$SNR_{out,MIW\ WBAN} = P_t - PL - P_{n,MIW\ WBAN} \quad (8)$$

where P_t is the transmitted power from the transmitter end of MIW WBAN in dBm, PL is the path loss caused due to MIW WBAN. Considering $P_t=1\text{mW}$ or 0dBm (as used in SAR calculations in Section VII) and using $PL = 15.4 \text{ dB}$ (maximum within the operating bandwidth of the abovementioned design), we get $SNR_{out,MIW\ WBAN} = 77.3 \text{ dB}$. Now, for demonstration purposes, consider BPSK modulation for calculation of bit error rate for MIW WBAN ($BER_{MIW\ WBAN}$) [20],

$$BER_{MIW\ WBAN} = 0.5 \text{erfc}(\sqrt{SNR_{out,MIW\ WBAN}}) \quad (9)$$

This leads to $BER_{MIW\ WBAN}=0$ for the above calculated $SNR_{out,MIW\ WBAN}$. Thus, the system provides a quite robust communication channel.

Further, if we assume $BER_{MIW\ WBAN} = 10^{-10}$ for a good quality communication channel, we get $SNR_{out,MIW\ WBAN} = 13 \text{ dB}$. This provides a signal-to-noise ratio margin ($SNR_{out,MIW\ WBAN,margin}=77.3\text{dB} - 13\text{dB}$) of 64.3 dB which serves three purposes: (a) adds robustness to the system in presence of any tolerance or path loss variation caused due to unaccounted factors, (b) adds sufficient margin for increase in noise levels, thereby, ensuring reliable performance even in highly noisy environments, and (c) provides ample margin to lower the transmitted power significantly.

For a quantitative demonstration of the above, consider that, 4.3 dB out of 64.3 dB is reserved for unaccounted factors leaving 60 dB of margin. In the absence of any additional noise, the transmitted power (P_t) set to 0 dBm for the above calculation can now go down to -60dBm (or as low as 1nW). Even if 30 dB out of 60 dB margin is reserved to tackle

increase in noise, it still allows 30 dB margin for transmitted power (leading to transmitted power level of 1 μW). Thus, reduction in path loss can add to robustness in highly noisy environments and reduce power consumption significantly while maintaining a high quality communication channel and robustness to unaccounted factors.

X. CONCLUSION

We introduced a new approach of MIW to realize WBANs that are superior over the state-of-the-art in terms of loss, power requirements, reliability, robustness, interference and security performance. The underlying operating principle was explained using basic theory and dispersion diagrams at an example frequency band of 40.4 MHz. Proof-of-concept numerical results were further demonstrated in two frequency bands centered around 40.4 MHz and 80.7 MHz, respectively. Results showed minimum loss and 10-dB absolute bandwidth of 5.4 dB and 11.8 MHz, and 5.3 dB and 25 MHz, respectively enabling extremely low loss and high data rate WBAN. A robust experimental set-up was then created using 3-D printed fixtures, electrically small resonant loops, and ground beef emulating biological tissues. Numerical and experimental results were in excellent agreement. Design guidelines were subsequently explored to enable the optimal implementation of MIW-enabled WBANs for diverse application scenarios. Important practical considerations, including effect of tilt in loops, anatomical shape of limbs, and effect of limb movements were evaluated demonstrating robustness of the design in such scenarios. In continuation of the above, possible events of loop failure and hypothetical non-uniform gap cases are brought forward with their potential impact on performance. A brief discussion covers benefits of MIWs over continuous connecting structures (such as microstrip line) for wearable WBAN. A SAR study was also conducted to confirm that MIW technology is safe for human use. In all cases, frequencies in the inductive region were identified as preferable. A quantitative comparison showed that MIW can exhibit over 63 dB lower loss vs. state-of-the-art WBANs (i.e. over 6 orders of improvement) at an example 10 cm to 40 cm distance between the transmitter and receiver. Loss performance was shown to further improve with increasing distance. Finally, bit error rate calculations demonstrated that MIW WBAN can form a reliable, robust and high quality communication channel. In addition, the same analysis also showed the impact of reduced path loss in improving robustness to noisy environments and bringing down the power requirements to as low as μW to nW as compared to ~mW in conventional state-of-the-art WBAN.

In future, emphasis will be laid on (a) improving impedance mismatch across the passband (to reduce the ripples and further improve performance), (b) implement and test the performance *in vivo*, (c) translate the MIW on conductive e-threads that will enable flexible, conformal, and seamless WBANs, and (d) analyze practical factors such as wearability and washability associated with the translation.

REFERENCES

- [1] K. Hasan, K. Biswas, K. Ahmed, N. S. Nafi, and M. S. Islam, "A comprehensive review of wireless body area network," *J. Netw. Comput. Appl.*, vol. 143, pp. 178–198, Oct. 2019.
- [2] B. Latré, B. Braem, I. Moerman, C. Blondia, and P. Demeester, "A survey on wireless body area networks," *Wirel. Netw.*, vol. 17, no. 1, pp. 1–18, Jan. 2011.
- [3] S. Movassaghi, M. Abolhasan, J. Lipman, D. Smith, and A. Jamalipour, "Wireless body area networks: a survey," *IEEE Commun. Surv. Tutor.*, vol. 16, no. 3, pp. 1658–1686, Third 2014.
- [4] M. Seyedi, B. Kibret, D. T. H. Lai, and M. Faulkner, "A survey on intrabody communications for body area network applications," *IEEE Trans. Biomed. Eng.*, vol. 60, no. 8, pp. 2067–2079, Aug. 2013.
- [5] H. Baldus, S. Corroy, A. Fazzi, K. Klabunde, and T. Schenk, "Human-centric connectivity enabled by body-coupled communications," *IEEE Commun. Mag.*, vol. 47, no. 6, pp. 172–178, Jun. 2009.
- [6] R. Cavallari, F. Martelli, R. Rosini, C. Buratti, and R. Verdone, "A survey on wireless body area networks: technologies and design challenges," *IEEE Commun. Surv. Tutor.*, vol. 16, no. 3, pp. 1635–1657, Third 2014.
- [7] N. Golestani and M. Moghaddam, "Theoretical modeling and analysis of magnetic induction communication in wireless body area networks (WBANs)," *IEEE J. Electromagn. RF Microw. Med. Biol.*, vol. 2, no. 1, pp. 48–55, Mar. 2018.
- [8] E. Shamonina, V. A. Kalinin, K. H. Ringhofer, and L. Solymar, "Magneto-inductive waveguide," *Electron. Lett.*, vol. 38, no. 8, pp. 371–373, Apr. 2002.
- [9] V. Mishra and A. Kiourti, "Electromagnetic components realized on conductive wires: a copper vs. e-thread comparison," in *2019 IEEE International Symposium on Antennas and Propagation and USNC-URSI Radio Science Meeting*, pp. 359–360, Jul. 2019.
- [10] V. Mishra and A. Kiourti, "Wrap-around wearable coils for seamless monitoring of joint flexion," *IEEE Trans. Biomed. Eng.*, vol. 66, no. 10, pp. 2753–2760, Oct. 2019.
- [11] E. Shamonina, V. A. Kalinin, K. H. Ringhofer, and L. Solymar, "Magnetoinductive waves in one, two, and three dimensions," *J. Appl. Phys.*, vol. 92, no. 10, pp. 6252–6261, Oct. 2002.
- [12] C. Furse, D. A. Christensen, C. H. Durney, "Electric and magnetic fields: basic concepts," in *Basic Introduction to Bioelectromagnetics 2nd ed.*, Boca Raton: CRC Press, 2009 pp. 30-34.
- [13] P. Soontornpipit, C. M. Furse, and You Chung Chung, "Design of implantable microstrip antenna for communication with medical implants," *IEEE Trans. Microw. Theory Tech.*, vol. 52, no. 8, pp. 1944–1951, Aug. 2004.
- [14] S. Gabriel, R. W. Lau, and C. Gabriel, "The dielectric properties of biological tissues: II. Measurements in the frequency range 10 Hz to 20 GHz," *Phys. Med. Biol.*, vol. 41, no. 11, pp. 2251–2269, Nov. 1996.
- [15] C. W. L. Lee, A. Kiourti, J. Chae, and J. L. Volakis, "A high-sensitivity fully passive neurosensing system for wireless brain signal monitoring," *IEEE Trans. Microw. Theory Tech.*, vol. 63, no. 6, pp. 2060–2068, Jun. 2015.
- [16] A. Kiourti and K. S. Nikita, "Numerical assessment of the performance of a scalp-implantable antenna: Effects of head anatomy and dielectric parameters," *Bioelectromagnetics*, vol. 34, no. 3, pp. 167–179, 2013.
- [17] R. Ketola, V. Mishra, and A. Kiourti, "Modeling fabric movement for future e-textile sensors," *Sensors*, vol. 20, no. 13, Jul. 2020.
- [18] FCC OET, "Evaluating compliance with FCC guidelines for human exposure to radio frequency electromagnetic fields," Bulletin 65, Washington, DC. Available: <https://www.fcc.gov/general/oet-bulletins-line>. [Accessed: 18-Feb-2020].
- [19] A. Thielens, R. Benarrouch, S. Wielandt, M. G. Anderson, A. Moin, A. Cathelin, and J. M. Rabaey, "A comparative study of on-body radio-frequency links in the 420 MHz–2.4 GHz range," *Sensors*, vol. 18, no. 12, p. 4165, Dec. 2018.
- [20] J. G. Proakis and M. Salehi, "Optimum receivers for AWGN channels" in *Digital Communications 5th ed.*, McGraw-Hill, 2008.



Vigyanhu Mishra (S'18) earned Bachelor of Technology degree in electronics and communication engineering from PDPM Indian Institute of Information Technology, Design and Manufacturing, Jabalpur, Madhya Pradesh, India, in 2012, and Master of Technology degree in radio frequency design and technology from Indian Institute of Technology, Delhi, India, in 2015.

He is currently pursuing his PhD in Electrical and Electronics Engineering from The Ohio State University, ElectroScience Laboratory, Columbus OH, USA, under the supervision of Dr. Asimina Kiourti. In past, he has held research positions on different research projects at Center for Applied Research in Electronics, Indian Institute of Technology, Delhi, India and has served as Engineer in Wireless Planning and Coordination Wing, New Delhi and Wireless Monitoring Organization, Ahmedabad, Ministry of Communication and IT, Government of India. He has authored 6 journal papers and 7 conference papers till date. He has worked on various aspects of electromagnetics and his current research interests include electromagnetics for wearable and biomedical applications.

Mr. Mishra has received several awards and fellowships including the IEEE Microwave Theory and Techniques Society (MTT-S) Graduate Fellowship for Medical Applications for 2019, USNC-URSI 2019 Travel Fellowship, and University Fellowship for the year 2017-18 by The Ohio State University. He is serving as a reviewer for IEEE Transactions on Antennas and Propagation.



Asimina Kiourti (S'10, M'14, SM'19) received the Diploma degree in electrical and computer engineering from the University of Patras, Patras, Greece, in 2008, the M.Sc. degree in technologies for broadband communications from University College London, London, U.K., in 2009, and the Ph.D. degree in electrical and computer engineering from the National Technical University of Athens, Athens, Greece, in 2013.

She is currently an Assistant Professor of Electrical and Computer Engineering at The Ohio State University and the ElectroScience Laboratory, Columbus, OH, USA. From 2013 to 2016 she served as a Post-Doctoral Researcher and then a Senior Research Associate at the ElectroScience Laboratory. During her career, she has authored over 55 journal papers, 80 conference papers, 11 book chapters and 10 patents. Her research interests include bio-electromagnetics, wearable and implantable antennas, sensors for body area applications, and functionalized e-textiles.

Dr. Kiourti has received several awards and scholarships, including the URSI Young Scientist Award for 2018, the IEEE Engineering in Medicine and Biology Society (EMB-S) Young Investigator Award for 2014, the IEEE Microwave Theory and Techniques Society (MTT-S) Graduate Fellowship for Medical Applications for 2012, and the IEEE Antennas and Propagation Society (AP-S) Doctoral Research Award for 2011. She is currently serving as a Senior Editor for the IEEE Open Journal of Antennas and Propagation and an Associate Editor for the IEEE Transactions on Antennas and Propagation and the IEEE Journal of Electromagnetics, RF and Microwaves in Medicine and Biology.